BioChip Journal
https://doi.org/10.1007/s13206-025-00206-1

ORIGINAL ARTICLE

UV Adhesive Hybrid Bonding for Sub-100-μm DLP-3D-Printed Microchannels

Seungmin Lee[1] · Bhargav Krishna Pullagura[1] · Youngbin Kim[1] · Chan Lee[1] · Abdi Mirgissa Kaba[1] · Boseok Huh[1] · Jintae Kim[1] · Sang Kug Chung[1] · Dohyun Kim[1]

Received: 23 November 2024 / Revised: 26 February 2025 / Accepted: 14 March 2025

Abstract

We present an effective and practical adhesive bonding method for integrating a 3D-printed microfluidic chip with a polymethylmethacrylate (PMMA) substrate. Digital-light-processing (DLP) 3D printing has been extensively used for prototyping microfluidic devices because intricate three-dimensional fluidic structures can be directly printed with high resolution and throughput. However, time-consuming post-processing is typically required for DLP-printed chips due to optical translucency, which impedes optical detection and microscopic observation. In addition, monolithic printing of small channels (< 100 μm) has proven particularly challenging due to difficulties in draining uncured resin. To address these problems, we developed an adhesive bonding technique that employs a transparent PMMA cover plate to enclose a DLP-printed open-channel chip, forming a hybrid PMMA-3D print device. This technique leverages vacuum-assisted removal of channel-filling UV adhesive. The resulting bond exhibited excellent burst strength, exceeding 869 kPa (> 8.58 atm), surpassing previously reported values. Furthermore, brightfield and fluorescence imaging revealed that the optical clarity of our hybrid chips was superior to that of chips fabricated entirely using a DLP 3D printer. Channel contamination due to adhesive was minimal, with a reduction in cross-sectional area being less than 6%. Notably, a sub-100-μm microchannel was successfully fabricated without clogging (76.1×50.9 μm^2 cross-section), significantly smaller than those achieved via monolithic DLP printing or traditional adhesive bonding. As proof of concept, we manufactured hybrid microfluidic devices for inertial focusing and droplet generation, fully functional without leakage. We anticipate that our rapid and effective hybrid bonding method will be widely adopted for the prototyping of microfluidic devices with sub-100-μm features, particularly those requiring optical quantification or microscopic investigation.

Keywords Hybrid bonding · Polymer microfabrication · Digital-light-processing (DLP) 3D printing · Polymethyl methacrylate (PMMA) · Inertial microfluidics · Droplet microfluidics

1 Introduction

Microfluidics promises to revolutionize biomedical fields covering biochemical analysis and synthesis, drug screening, cellular biology studies, and disease diagnosis, owing to its ability to perform sensitive, high-throughput analyses with minimal reagent and sample consumption [1, 2]. A key aspect of microfluidics contributing to its rapid growth is the ability to handle a minute volume of liquid (pL ~ μL). Realizing this capability requires specialized machining techniques that can fabricate fluidic structures and components including channels, reactors, valves, and pumps at nano- to microscales [3]. In the early days, microfluidic devices were manufactured with silicon and/or glass through traditional cleanroom-based photolithography techniques [4, 5]. However, the opaqueness (silicon), rigidity, high material costs, and the need for a cleanroom, expensive fabrication equipment, and skilled operators diverted researchers toward PDMS-based soft lithography [6]. Although PDMS remains an indispensable substrate material, it has limitations including hydrophobicity, gas permeability, and a labor-intensive fabrication process that is challenging to scale up for large-volume commercialization [7]. Moreover, soft lithography requires photolithography for master-mold fabrication. It is fundamentally limited to 2.5 dimensions,

✉ Dohyun Kim
dohyun.kim@mju.ac.kr

[1] Department of Mechanical Engineering, Myongji University, 116 Myongji-ro, Yongin 17058, Republic of Korea

Published online: 04 April 2025

even when multiple PDMS layers are stacked, which precludes the benefits of genuine 3D device architectures [8]. In addition, most mass-produced microfluidic devices are fabricated using hard plastic materials such as polymethyl methacrylate (PMMA) [9, 10], polystyrene (PS) [11], polycarbonate (PC) [12, 13], cyclic olefin copolymer (COC) [14] through industry-scale manufacturing methods like injection molding [15] and hot embossing [16]. The properties of PDMS differ largely from those of hard plastics, complicating technology translation into mass production.

3D printing, a layer-by-layer additive manufacturing technique, has emerged as a technology driver in the microfluidics field by addressing the limitations of these traditional fabrication methods [17–21]. The advantages of 3D printing are: (1) the fabrication of true 3D free-form structures (e.g., 3D spiral microchannels with trapezoidal cross-sections); (2) cleanroom-free operation; (3) the availability of affordable desktop 3D printers (starting from a few hundred US dollars); (4) mechanical properties similar to those of hard plastics; (5) straightforward world-to-chip interfacing through integrated fluidic couplings (e.g., Luer-Lok); and (6) direct fabrication from a CAD design with minimal manual intervention (e.g., alignment, bonding, and punching) [8]. Among various 3D-printing technologies, such as fused deposition modeling (FDM), selective laser sintering (SLS), laminated object manufacturing (LOM), multijet modeling (MJM), and digital light processing (DLP), DLP printing has proven to be particularly effective for microfluidic-device fabrication. It offers several advantages over the other 3D printing techniques, including: (1) superior printing resolution (as low as 2 μm in the *XY* plane and 1 μm in the *Z* direction); (2) better surface finish and transparency (especially compared with extrusion-based FDM); (3) simpler support removal (i.e., draining uncured resin); and (4) faster printing [22–24]. Consequently, the number of DLP-printed microfluidic devices has rapidly grown in recent years [25].

Despite these advantages, DLP 3D printing is not without shortcomings: (1) cytotoxicity and limited biocompatibility; (2) gas impermeability (for cell culture applications); and (3) difficulties in multi-material printing [18, 26]. However, a major obstacle to its widespread adoption is its limited optical transparency compared to popular substrates like PMMA, PC, and PDMS [7, 19]. Transparency is critical for microfluidic devices, which are frequently used for optical detection and microscopy imaging [27, 28]. The reduced transparency in a DLP-printed structure is primarily due to light diffraction and scattering caused by surface roughness and volume defects [28, 29]. Various approaches have been attempted to improve transparency. Mechanical polishing (e.g., sanding, alumina polishing) has been employed [30], but this process is labor-intensive, and the surface finish highly depends on the operator's skill. In addition, dimensional changes (i.e., thickness reduction) are often inevitable [8]. Chemical polishing has also been explored, but it generates toxic and flammable solvent fumes [31]. External and internal polymer coatings (e.g., PDMS coatings and acrylic spray) have been used to enhance transparency [32]. However, in-channel coatings reduce cross-sections, and spraying polymers can pose health risks (e.g., polyurethane coatings) [33]. Moreover, drying coatings can take a long time (> 1 day) [30]. Refractive-index (RI)-matching coatings (e.g., oil) have improved transparency by creating a smooth liquid surface, but issues with coating reliability (e.g., dust accumulation, wiping by contact) persist [8]. Printing onto a transparent substrate (e.g., glass, PMMA) [34, 35] and inserting a substrate during printing have also been suggested [36, 37]. However, tedious *Z*-axis calibration is required (e.g., FDM printing), and attaching a substrate to a build platform can damage the vat window (i.e., DLP printing). Our group has reported a systematic surface-treatment method based on sanding, alumina polishing, and RI matching [8]. However, the achieved transparency was still insufficient for applications where optical clarity is crucial, such as particle image velocimetry (PIV) and fluorescence-based quantitative immunoassay [38, 39].

Another well-known challenge in DLP printing is the difficulty in draining uncured resin [40, 41]. The hydraulic resistance of viscous resin in long, narrow microchannels, rather than printing resolution, is often the major limiting factor in fabricating high-resolution microfluidic features (say, < 200 μm). In addition, partial resin curing due to light bleeding from the channel "ceiling" exacerbates the drainage problem by reducing channel height and increasing resin viscosity [42]. Therefore, we propose a new fabrication method that combines DLP printing of an open-channel architecture with adhesive bonding of a PMMA cover plate to tackle both optical transparency and resin-drainage issues. Removing uncured resin from an open-channel chip (i.e., a microfluidic chip without a ceiling) becomes significantly easier than from enclosed ones [30, 43]. Afterward, the open channels are sealed with a pristine PMMA substrate to form an enclosed microfluidic device.

Bonding is a critical step in the proposed fabrication method. The bond must reliably join two dissimilar surfaces (i.e., a 3D-printed chip and PMMA) without degrading transparency, deforming microfluidic features, contaminating inner surfaces, or compromising the ability to sustain hydrodynamic pressure under desired operating conditions [44–46]. Irreversible bonding of PDMS via oxygen-plasma treatment is effective and prevalent in microfluidic devices [6]. However, achieving reliable bonding of hard plastics remains elusive without a universal solution. Bonding techniques are broadly categorized into direct and indirect methods [44–46]. Among direct bonding methods, thermal fusion bonding creates permanent bonds using only heat and pressure, but it is sensitive to surface roughness and

cleanliness and can deform microfeatures. Moreover, thermal bonding is most effective with identical surfaces (e.g., PMMA to PMMA) [47]. Solvent-assisted bonding softens and activates surfaces to allow polymer chains to intertwine across the interface [48]. Although dissimilar surfaces can be bonded [48], the use of toxic solvents, feature distortion, and channel clogging are problematic [44]. There were few reports on solvent-assisted bonding of PMMA and FDM-printed chips made of PLA (polylactic acid) [48] and ABS (acrylonitrile butadiene styrene) [49]. However, the resolution and surface quality of FDM-printed chips were inferior to those produced by DLP printing. Bonding based on physical surface modification (e.g., UV, ozone, oxygen-plasma treatment) activates the surface by breaking chemical bonds and generating polar surface groups. However, the bonding strength is moderate, and the types of bondable surface pairs are limited. Ultrasonic bonding and laser welding use acoustic and light energy, respectively, to locally liquefy plastics, forming bonds upon solidification [44, 46]. However, these methods require energy directors for ultrasonic bonding (e.g., sharp edges) and light-absorbing materials for laser welding (e.g., titanium film or carbon blacks), hindering their broad adoption. In addition, expensive equipment (e.g., ultrasonic welder, and laser with an *XY* stage) is necessary.

Among indirect bonding techniques, bonding based on chemical surface modification activates surfaces to harness functional groups and uses covalent linking chemistry, such as (3-aminopropyl)triethoxysilane (APTES) and 3-(trimethoxysilyl)propyl methacrylate (TMSPMA), to bond two like or dissimilar surfaces [44, 46, 50]. While this approach offers excellent bonding strength, the types of bondable surface pairs are limited, and multiple processing steps (including physical surface modification) complicate commercialization [46]. Adhesive bonding, a versatile indirect bonding method, employs an intermediate gluing layer, either in solid or liquid form with a large selection of materials [51]. This approach is simple, universal, and rapid, capable of irreversibly joining similar surfaces such as PDMS-PDMS [52], PMMA-PMMA [9], and COC-COC [14], as well as a variety of dissimilar surface pairs including PMMA-PC [53], PMMA-PDMS [54, 55], PDMS-polyimide [56], PDMS-3D printed chip [57], PDMS-PET (polyethylene terephthalate) [58], PDMS-PS [58], and PMMA-printed circuit board [59]. In addition, adhesive bonding can be achieved at moderate temperatures with minimal equipment such as a UV-light source, rollers, and clamps. In this study, we opted to use liquid adhesive because the bonding strength of solid adhesives (e.g., pressure-sensitive tapes, lamination films) is generally weaker, as evidenced by Saffman-Taylor instability [44, 60]. While previous studies reported bonding PMMA and FDM-printed chips using liquid adhesives [35, 43, 48], these methods also suffer from mediocre printing resolution and surface quality [7, 24, 61]. To the best of our knowledge, this is the first study to investigate adhesive bonding between a chip printed with a high-resolution DLP printer and a PMMA substrate.

Liquid adhesive wets two joining surfaces and is cured to create bonds under UV light or heat [44, 46]. A key consideration with liquid adhesive is the risk of channel occlusion due to capillary action [30, 62]. Various approaches have been employed to prevent channel clogging including a stamp-and-stick method (i.e., contact printing) [30, 52], glue guide channels (or sacrificial channels) [63, 64], capillary-mediated interstitial adhesive injection [62], and channel shielding with tapes before applying liquid adhesive [65]. However, these methods increased the complexity of the bonding process and chip designs, often with limited success. Here, we propose a simple yet effective method of vacuum-assisted removing liquid adhesive before curing. Among liquid adhesives frequently used in microfluidics such as PDMS [52, 66], epoxy [56], and SU-8 [67], UV-curable resins have garnered much attention due to their strong adhesion to various plastic surfaces [68] and excellent optical transparency [69]. In this work, NOA-86H, a UV-curable adhesive, was employed to form hybrid microfluidic devices comprising PMMA cover plates and DLP-printed open-channel chips.

In this work, we present a detailed fabrication process based on DLP printing combined with vacuum-assisted removal of UV-curable adhesive. We then compare the optical transparency of a fabricated hybrid device with that of a monolithically printed chip and evaluate the bond strength of a hybrid device. The variation in the channel cross-sectional area after bonding is characterized to demonstrate the precision of our fabrication method. In addition, we fabricate a sub-100 μm microchannel, a particularly challenging feat using existing DLP printing and bonding techniques. Lastly, as a proof of concept, we fabricate and characterize the performance of two popular microfluidic devices, an inertial focusing device and a droplet microfluidic device.

2 Materials and Methods

2.1 Materials and Reagents

All chemicals were reagent grade. Isopropyl alcohol (IPA, 99.5%) was purchased from Samchun Chemicals (Pyeongtaek, South Korea), and 18.2 MΩ cm DI water was obtained from a DI water facility (Youngin Chromass, Anyang, South Korea) in Myongji University. IPA and DI water were employed to clean residual adhesives from DLP-printed chips and the channels of hybrid PMMA-DLP print devices. PR-48 resin, an open-source acrylate resin developed by Autodesk, was purchased from CPS (Boulder, CO, United States), and served as both the DLP printing material

and a UV adhesive. Another UV adhesive, NOA-86H from Norland Products (Jamesburg, NJ, United States), was also employed for bonding. NOA-68 (Norland) and an instant glue (V-tech Strong Instant Adhesive, Youngil TS, Siheung, South Korea) were used to attach Luer fittings to the outlet ports of hybrid devices. A 0.5-mm-thick PMMA substrate (Acryl Choi-ga, Seoul, South Korea) was used as a cover plate for open-channel microfluidic chips. Green-fluorescence polystyrene microbeads (40-μm in diameter) were purchased from Abvigen (#ABWG-21-4000, Newark, NJ, United States) for optical-quality characterization and use in inertial microfluidics applications.

2.2 Fabrication Process Flow

UV-adhesive hybrid bonding of a DLP-printed chip and a PMMA cover plate is carried out as follows:

Step 1. A PMMA substrate is machined using a 50-W CO_2 laser cutter (Mini 24, Epilog, Golden, CO, United States) to create a cover plate with inlet and outlet holes (Fig. 1a). The machined PMMA cover plate is then thoroughly cleaned using IPA and DI water. After cleaning, the cover plate is dried using a nitrogen blow. Next, 500 μL of liquid adhesive, either NOA-86H UV glue or PR-48 resin, is pipetted onto the PMMA cover plate. The cover plate is then spun at 1000 rpm for 90 s, with a ramp rate of 100 rpm/s using a spin coater (SC-100RPM, Rhabdos, Seoul, South Korea) to evenly distribute the liquid adhesive on the PMMA surface.

Step 2. A microfluidic chip with open channels is designed using SolidWorks CAD software (Dassault Systèmes, Vélizy-Villacoublay, France) and printed using a high-resolution DLP 3D printer (Max X27, Asiga, New South Wales, Australia) with PR-48 resin and its slicer software Composer V1.3 (Asiga). After printing, residual resin on the chip is washed by placing the chip inside a beaker filled with IPA and cleaning it in an ultrasonic bath (UC-20, Jeio Tech, Daejeon, South Korea). Post-printing curing is then performed by exposing the chip to UV light using a UV irradiator (Flash Cure Box, Asiga) for 30 min. A 3D-printed chip and PMMA cover plate are manually aligned and brought into contact for temporary bonding (Fig. 1b).

Step 3. The temporarily bonded chip assembly is clamped using paper clips (iField Co., Incheon, South Korea) on all four edges (Fig. 1c). As intended, the liquid adhesive filled the interstitial space (i.e., the gap) between the 3D-printed chip and the cover plate. However, capillary action inevitably causes some adhesive to enter the microchannels.

Step 4. The adhesive inside the channel is removed using a suction pump (BF-101, BioFree, Bucheon, South Korea) as presented in Fig. 1d. The suction time depends on the complexity of a microchannel network and the viscosity of the adhesive. It usually takes 10 min for PR-48 and 30 min for the more viscous NOA-86H. The microchannels are further cleaned by vacuum suction using IPA and DI water for 15 min and 2 min, respectively. Caution must be exercised during this step, as a slight release of pressure from

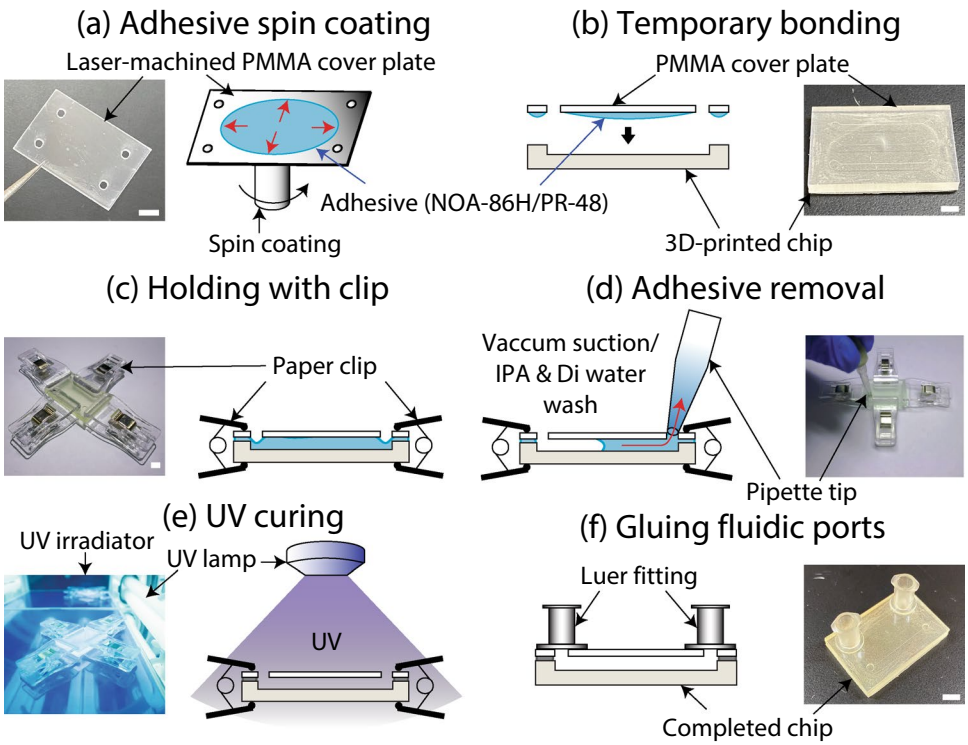

Fig. 1 Fabrication process flow. **a** A UV adhesive (NOA-86H or PR-48) is spin-coated onto a laser-machined PMMA cover plate. **b** The cover plate is manually aligned and temporarily bonded to a DLP-printed chip with open channels. **c** The chip-cover plate assembly is tightly clamped using paper clips. **d** The adhesive drawn to the channel by capillary action is removed by vacuum suction and cleaned using isopropyl alcohol and DI water. **e** The chip-cover plate assembly is exposed to UV light inside a UV irradiator. The adhesive is cured to bond the chip and the cover plate permanently. **f** Luer fittings are attached to the PMMA cover plate using instant glue and a UV adhesive

the paper clips can cause channel contamination from the adhesive initially filling the chip-cover plate gap.

Step 5. The liquid adhesive is cured inside the same UV irradiator for 10 min (Fig. 1e). This photocuring process permanently bonds the cover plate and DLP-printed chip, forming an enclosed microfluidic device.

Step 6. Lastly, Luer fittings (part# 10000014, Microfluidic ChipShop, Jena, Germany) are attached to the inlet and outlet ports of the machined PMMA cover plate using instant glue as shown in Fig. 1f. A UV adhesive NOA-68 is applied to the seam around the Luer fittings and then cured under UV light for 30 min to permanently seal the interface between the Luer fittings and the cover plate.

2.3 Optical Characterization of Hybrid Chips

The transparency of hybrid PMMA-DLP print chips was qualitatively evaluated using brightfield and fluorescence imaging techniques. The analysis was performed on an upright microscope BX-50 (Olympus, Tokyo, Japan) equipped with a high-speed sCMOS camera (Edge 5.5, PCO, Kelheim, Germany). A microfluidic chip featuring a straight channel with nominal dimensions of 500 µm × 500 µm × 30 mm was monolithically printed using our 3D printer. The uncured resin was cleared using vacuum suction. Afterward, the same post-printing process described in Step 2 of Sect. 2.2 was followed to complete fabrication. No surface-treatment like sanding and polishing was applied [8]. The thickness of the channel ceiling was 0.5 mm. A second chip of identical dimensions but featuring an open channel was also printed. The key difference was the bonding of a 0.5-mm thick PMMA cover plate to the chip, matching the 0.5-mm ceiling thickness of the monolithically printed chip. A 0.1% v/v solution of 40-µm fluorescent polystyrene microbeads (Abvigen) was injected into both chips. Brightfield and fluorescence images of the beads were then captured under the microscope for visual comparison.

2.4 Dimensional Accuracy Evaluation

For the dimensional accuracy test, open-channel chips with nominal dimensions of $0.2 \times 0.1 \times 3$ mm^3 were fabricated. The cross-sectional dimensions were first measured using a laser-scanning surface profilometer (VK-X3000, Keyence, Osaka, Japan) before bonding. However, the surface profilometer was not compatible with bonded chips. Therefore, channel cross-sections were imaged and measured using a microscope. To prepare samples for imaging, the chips were cut at the midpoint using the CO_2 laser machine after bonding with NOA-86H or PR-48. The cut surfaces were thoroughly cleaned using IPA and a nitrogen blow. The channel cross-sections were then imaged, and measured using an upright microscope BX-40 (Olympus, Tokyo, Japan) equipped with an sCMOS camera (Quantalux CS2100M-USB, Thorlabs, Newton, NJ, United States). All measurements were calibrated with a microscope micrometer (Alpha Science, Seoul, Korea). Changes in cross-sectional areas, before and after bonding, were calculated to assess dimensional accuracy.

2.5 Bonding Strength Measurement

A burst test setup was custom-built as exhibited in Fig. 2. A straight-channel chip (nominal channel dimensions of $2 \times 0.1 \times 3$ mm^3 and chip dimensions of $15 \times 40 \times 2$ mm^3, see Fig. S1 in the Supplementary Information) was designed and fabricated using our described fabrication technique. A syringe pump (Legato 100, KD Scientific, MA, USA) equipped with a 10-mL syringe (HENKE-JECT Luer lock, Henke-Sass Wolf, Tuttlingen, Germany) was used to exert pressure into the two test microfluidic chips (one bonded with NOA-86H and the other with PR-48) through the inlet port using 0.8-mm-ID Tygon tubing (PharMed BPT, Saint-Gobain, Courbevoie, France). For visualization, a red food-color dye solution (0.01% w/v, Chunwoo Food Manufacturing, Seoul, South Korea) was used as the test fluid. The flow rate was set at 1 mL/min. An in-line pressure sensor (MPS-4S, Elveflow, Paris, France) was connected to the chip outlet to measure hydraulic pressure in real-time via a 1/16 Teflon tubing (Sungjin Rubber Industrial CO., Seoul, South Korea). The sensor was connected to a PC through a dedicated sensor reader (MSR, Elveflow) for data acquisition. A metering valve (P-446, IDEX Health & Science, Oak Harbor, WA, United States) was connected to the pressure sensor through the same Teflon tubing. Initially, the metering valve was fully open to allow fluid flow. Once a proper flow was observed, the valve was tightly closed to increase

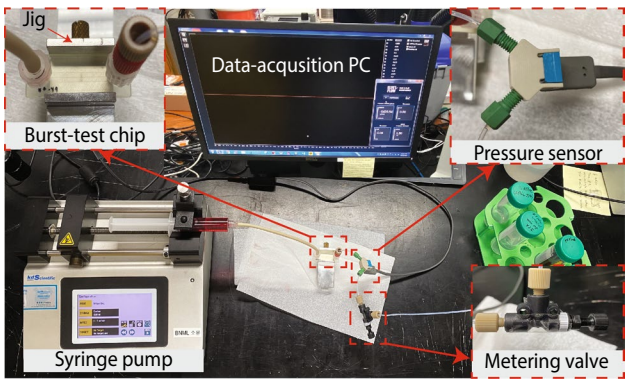

Fig. 2 Custom burst-test setup. The test chip's channel is pressurized through its inlet using a syringe pump, set to a flow rate of 1 mL/min. The chip's outlet is connected to an in-line pressure sensor that measures burst pressure in real time. The pressure sensor is connected to a metering valve, which controls the hydraulic pressure. The sensor is electrically connected to a PC for data acquisition

the pressure within this dead-end fluidic network. The pressure was then recorded using the sensor.

2.6 Design, Fabrication, and Characterization of an Inertial Focusing Device

An inertial focusing microfluidic device, comprising 33 asymmetrically curved segments, was designed and fabricated (Fig. 3). Each curved segment is 1680-µm long with a radius of curvature of 640 µm and a maximum channel width of 440 µm. Two consecutive segments are linked by a 200-µm-wide curved channel (a radius of curvature = 400 µm). The overall channel depth is 200 µm. To minimize the device footprint, the microchannel is folded twice to form three groups of curved segments. Consecutive groups are interconnected by 200-µm-wide, 5-mm-long straight channels. A 200-µm-wide, 9-mm-long straight channel section follows the last curved segment to facilitate imaging-based characterization of focusing performance. The fabrication process adhered to the steps outlined in Sect. 2.2.

Experimental verification of an inertial focusing device was conducted using 40-µm fluorescence beads (Abvigen). The concentration of the bead solution was 0.1% (w/v), with 2% (v/v) NP-40 detergent (Sigma, Burlington, MA, United States) added to minimize bead adsorption on the channel surfaces. A syringe pump (Legato 100) was employed to generate flow. Bead focusing was observed using the same upright microscope BX-50, equipped with a high-speed sCMOS camera (Fig. S2). Bead migration was captured at 100 frames per second (fps), and streamline images were synthesized using ImageJ (National Institutes of Health, Bethesda, MD, United States) from 500 frames (total of 5 s). The bead-stream width was quantified by calculating FWHM (full-width-half-maximum) values using a Gaussian peak-fitting function in OriginPro 2024 software (OriginLab, Northampton, MA, United States). The pressure was measured using an in-line pressure sensor (EIPS345, Fluigent, Le Kremlin-Bicêtre, France), which has a measurement range of 138 kPa and a resolution of 0.14 kPa.

2.7 Microfluidic Water-in-Oil Droplet Generation

The droplet generator has a flow-focusing configuration, as displayed in Fig. 4. The microfluidic device has two inlet ports, one for the continuous phase (oil, Inlet#1) and the other for the dispersed phase (water, Inlet#2), and one outlet port for collecting generated water-in-oil (W/O) droplets (Outlet). Two side channels stemming from Inlet #1 symmetrically inject oil into the cross-flow junction at the flow rate of Q_c. Water is injected from Inlet #2 into the junction at the flow rate of Q_d. All inlet channels are 300 µm in width. Monodisperse W/O droplets migrate through the outlet channel and are retrieved from the outlet. The outlet channel is 350-µm in width, slightly wider than the inlet channels. All channels are 325-µm deep, and the chip's overall footprint is 45 × 25 mm^2.

The fabrication process of the droplet generator is similar to that outlined in Sect. 2.2. However, there are two key differences: (1) the 3D-printed chip featuring embedded inlet

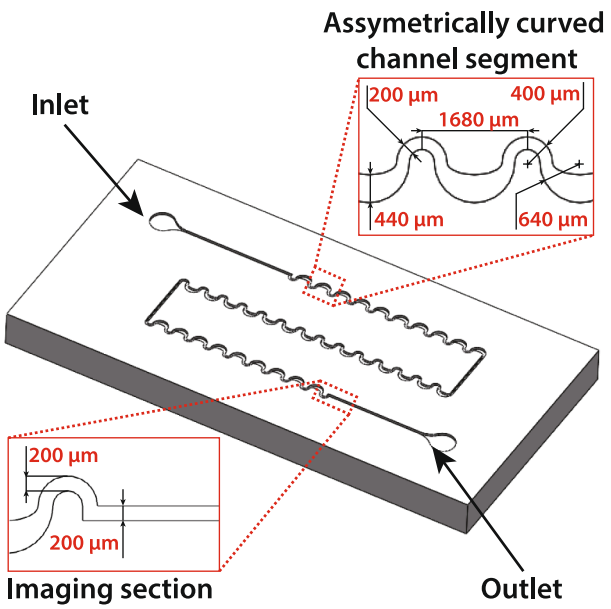

Fig. 3 Design of a particle-focusing device. The device comprises 33 asymmetric curved segments. Each segment features a radius of curvature of 640 µm, a maximum channel width of 440 µm, and a segment length of 1680 µm (top inset). A straight section (200-µm wide and 9-mm long) follows the last curved segment (bottom inset), designed for imaging inertial-focusing results

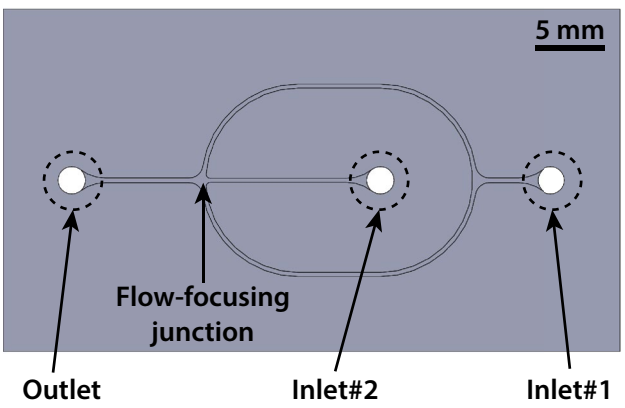

Fig. 4 Design of a microfluidic droplet generator. The device layout includes two inlets: one for the continuous phase (oil, Inlet#1) and another for the dispersed phase (water, Inlet#2). The microchannel for the continuous phase splits into two channels that converge with the channel for the dispersed phase at the flow-focusing junction. The generated water-in-oil droplets are collected from the outlet (Outlet)

and outlet holes was positioned on top, while the PMMA cover plate was placed at the bottom for microscopic observation of droplet generation from below (opposite to the design of the inertial focusing chip); (2) the top surface of the 3D-printed chip underwent a brief surface treatment to improve optical transparency for illumination from above. The surface-treatment process followed the method described in our previous work, with the exception that refractive-index-matching oil was not applied [8]. The polished chip was then bonded to a 0.5-mm-thick PMMA cover plate. Luer fittings (Microfluidic ChipShop) were attached to the inlet and outlet ports on the top surface of the 3D-printed chip, completing the fabrication process. The Luer fittings were not embedded in the 3D-printed model unlike previous reports [17] due to surface-treatment steps (e.g., sanding and alumina polishing).

The continuous-phase fluid was silicone oil (KF-96 100 cs, Shinetsu, Tokyo, Japan), while DI water served as the dispersed phase. A custom experimental setup was constructed for droplet generation (Fig. S3). Two syringe pumps (Legato 100) were used to inject the liquids into the microchannels. Droplet generation was observed using an inverted microscope IX70 (Olympus) equipped with a CCD camera (CoolSnap HQ^2, Teledyne Photometrics, Tucson, AZ, United States). The pressures in both the dispersed-phase and continuous-phase channels were simultaneously measured using a pair of in-line pressure sensors (EIPS345). Since the wetting properties of water and oil on the microchannel surface play a crucial role in droplet formation, and our device features two heterogeneous inner channel surfaces [70], we measured contact angles of water on a PMMA and a 3D-printed PR-48 surface using a goniometer (Smart Drop, FemtoBiomed, Seongnam, South Korea). The measured contact angles for PMMA and 3D-printed acrylate (PR-48) surfaces were similar (125.4° and 119.2°, respectively, Fig. S4), indicating that droplet-generation behavior in our device would be comparable to that in microchannels made entirely of either PMMA or 3D-printed PR-48 material.

3 Results and Discussion

3.1 Optical-Quality Characterization

Considering that microscopic imaging and optical measurement are routinely used in many microfluidic applications, the optical quality, specifically transparency for both brightfield and fluorescence, was qualitatively analyzed. As illustrated in the middle and bottom panels of Fig. 5, both brightfield and fluorescence images for the hybrid chip were significantly sharper and clearer than those of the monolithically printed chip. It was particularly difficult to recognize the beads in the fluorescence image of the monolithically

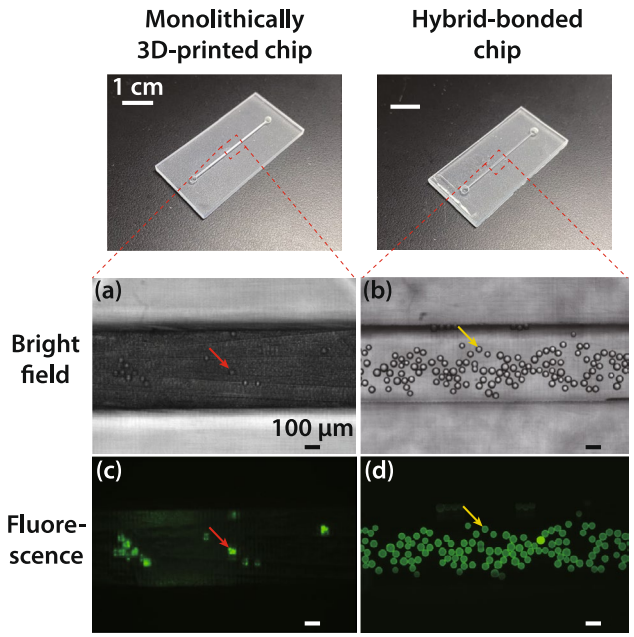

Fig. 5 Comparison of optical qualities between monolithically 3D-printed and hybrid microfluidic chips. Brightfield (**a**, **b**) and fluorescence microscopy images (**c**, **d**) visualize 40-µm fluorescence microbeads. The beads are marked by arrows. Superior clarity and higher resolution images were obtained for the hybrid chip (**b**, **d**), compared to the monolithically 3D-printed chip (**a**, **c**)

3D-printed chip (the arrow in Fig. 5c) [27]. Conversely, the fluorescence image of the hybrid chip clearly showed the beads (the arrow in Fig. 5d). These results indicate that our fabrication technique offers substantial optical-quality advantages over conventional monolithic DLP printing methods [7, 17–21].

3.2 Dimensional Accuracy of Hybrid Chips

A critical limitation of liquid adhesive bonding is channel occlusion [30, 71]. Bonding with adhesive tapes or lamination films [9, 60] can also clog microchannels depending on channel dimensions, tape material, and thickness. However, channel clogging is more severe with liquid adhesive due to their tendency to infiltrate microchannels by capillary action [62]. To address this problem, we explored various strategies to minimize clogging, as reported in the literature [30, 52, 62–65].

We initially explored the stamp-and-stick method (i.e., contact printing) to mitigate adhesive wetting of the channels. This approach involves spin-coating a liquid adhesive onto a transfer substrate. Subsequently, a 3D-printed open-channel chip is pressed onto this substrate to selectively "transfer" the adhesive pattern onto the elevated surfaces of the chip. Finally, the chip is brought into contact with a cover plate, and the adhesive is cured using UV light. However,

achieving a uniform adhesive coating on any of commonly used substrate materials, including PMMA, PC, and glass, was challenging due to uneven wetting or beading [56]. In addition, separating the 3D-printed chip from the transfer substrate without significant force or twisting motion was difficult due to surface tension. Similar problems of splitting two plastic substrates in the stamp-and-stick method have been reported [52]. This forceful and abrupt separation often led to uneven adhesive coating on the elevated surfaces and, consequently, bonding failures. Moreover, liquid adhesive still managed to spread into the channels despite using contact printing. We also experimented with the glue guide channel (or sacrificial channel) method, where additional fluidic structures are incorporated to guide the interstitial spreading of adhesive and prevent contamination of the main channels [63, 64, 72]. Nevertheless, even after several design attempts, this approach did not effectively prevent channel clogging.

Our simple yet effective solution to address channel clogging relies on vacuum suction to remove adhesive infiltrated into the channel. A similar approach was reported for bonding a CNC-machined PMMA microfluidic chip and a PMMA coverslip [73]. However, our process is more straightforward because it does not require filling the microchannel and gap between the two surfaces with liquid adhesive using nitrogen gas before removing the adhesive from the channel using vacuum suction, as conducted in previous work [73]. Notably, this is the first instance of using vacuum suction to bond a 3D-printed chip, which can incorporate more complex microfluidic features than the earlier CNC-machined PMMA chip, to a PMMA cover plate. During suction, the 3D-printed chip and cover plate are securely clamped to prevent leakage of liquid adhesive from the gap. Two critical process variables are the complexity of the microchannel network and the adhesive viscosity. More intricate channels and more viscous adhesives pose greater challenges in removing adhesives due to increased hydraulic resistance [7, 17].

We initially evaluated adhesives NOA-68 [69] and NOA-86H [57] due to their previous application in fabricating microfluidic devices, strong adhesion to plastic surfaces, and excellent transparency. However, NOA-68 was found to be unsuitable due to its high viscosity (4500–5500 cps) which made it extremely difficult to remove the adhesive from the channels. Consequently, NOA-86H with a lower viscosity (250–350 cps), was selected. As a control, we also tested PR-48, the resin used for printing our devices. It has a viscosity comparable to NOA-86H (400 cps) and was expected to adhere well to the chip surface as the chip was printed with the same resin. Both adhesives were removed relatively quickly (< 5 min) when the microchannel is wide and short, such as the transparency test chip with a straight channel of the dimensions $0.5 \times 0.5 \times 3$ mm^3 (Sect. 2.3). However, the resin removal took longer (20–30 min) for narrow and long channels such as those with dimensions of $0.2 \times 0.2 \times 3$ mm^3 on an inertial focusing device (Sect. 2.6). Therefore, the viscosity of the adhesive should be minimized to facilitate the fabrication process.

Before bonding, the measured channel cross-section of Chip#1 (fabricated using NOA-86H) was 173×102 μm^2, while that of Chip #2 (fabricated using PR-48) was 176×101 μm^2. The smaller channel size compared to the original CAD design (200×100 μm^2) may be attributed to the loss of a line of pixels (~ 27 μm wide) caused by the limited fidelity of the projection optics [28, 74]. After bonding, the channel dimensions became 164×105 μm^2 for Chip#1 and 169×109 μm^2 for Chip#2 (Fig. 6). This indicates a slight alteration in the channel cross-sections after bonding, with a 2.1% decrease for Chip#1 and a 3.6% increase for Chip#2. The reduction in-channel width is likely caused by the adhesive coating on the channel inner surface. The increase in channel height (+2 μm for Chip#1 and +8 μm for Chip#2) is likely due to the cured adhesive which is filling the gap between the 3D-printed chip and the PMMA cover plate. The thicker adhesive layer in Chip#2 could be attributed to

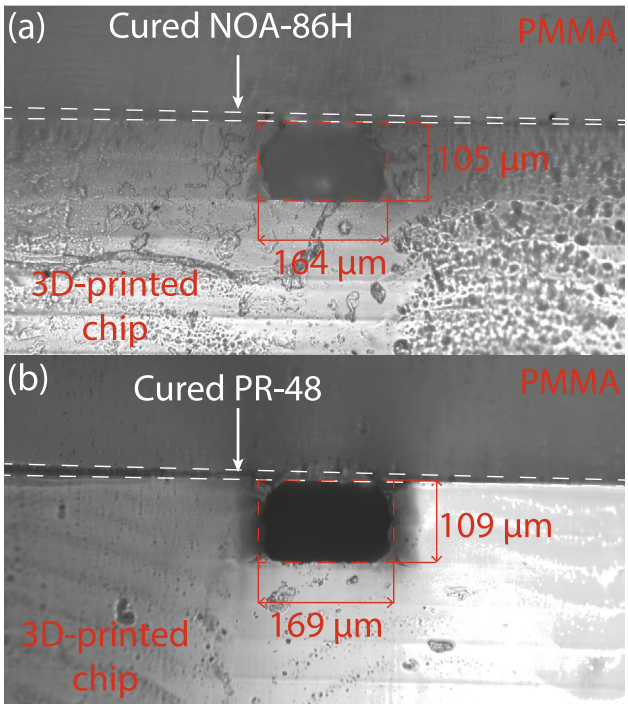

Fig. 6 Dimensional accuracy of our bonding method. The channel cross-sections of microfluidics chips bonded using **a** NOA-86H UV adhesive (Chip#1) and **b** PR-48 3D-printer resin (Chip#2). The cross-sectional changes from the 3D-printed originals were +2.1% for Chip#1 and − 3.6% for Chip#2, indicating comparable dimensional accuracy. The increase in-channel height (+2 μm for Chip#1 and +8 μm for Chip#2) is attributed to the adhesive filling the gaps between the 3D-printed chip and the cover plate

the higher viscosity of PR-48. In addition, the rounded corners observed in the rectangular cross-section of both chips can be attributed to capillary action. The dimensional accuracy, with an average variation of 2.97%, was deemed superior to the previous work involving the transfer and direct bonding of 3D-printed chips with glass cover plates. In this previous work, channel dimensions smaller than 250 µm (i.e., 200 × 200 µm^2 and 150 × 150 µm^2) were completely occluded [30].

For DLP printing of our open-channel architecture, major printing parameters were as follows: layer thickness (i.e., slice thickness) = 10 µm, layer offset (i.e., *Z* compensation) = 263 µm, exposure time = 2.3 s, and build direction = top-up orientation [8]. Additional detailed parameters are provided in Table S1. A general observation is that shorter exposure times and larger layer thicknesses tend to reduce *X*- and *Y*-dimensional errors [75]. Furthermore, *Z*-dimensional errors can be minimized by increasing layer thickness and decreasing layer offset [27]. However, excessive layer thickness may result in a staircase effect, deviating from a smooth 3D surface, while excessively low exposure times can lead to printing failures, such as layer delamination or under-cured microfeatures. To achieve the most accurate replication of nominal dimensions, the printing parameters were experimentally optimized. In conventional monolithic DLP printing, parameter optimization would be more complex compared to our method, as overcuring must be considered. Overcuring reduces channel height and, in some cases, leads to channel occlusion.

3.3 Realization of a DLP-Printed Sub-100 µm Microchannel

Fabricating a sub-100-µm channel using a commercial DLP printer and off-the-shelf resin is extremely challenging due to the limited fidelity of the projection optics [28, 74] and, more critically, the difficulties in draining partially cured resin from microchannels [7, 17–20, 41, 42]. In our approach, the printed channel is open (i.e., not enclosed), which renders clearing uncured resin much easier [30]. In addition, removing residual adhesives from inside the channel after temporary bonding is easier because the adhesive is not exposed to UV or partially cured, as in conventional monolithic 3D printing.

Although sub-100-µm channels have been printed in some previous studies, these typically required custom resin formulations, high-temperature sintering, custom 3D printers, or exceptionally large channel heights [74, 76, 77]. While these approaches are technically intriguing, their widespread adoption in biology or biochemistry labs, which often lack engineering expertise, would be elusive. Sub-100-µm PDMS microfluidic channels based on open-channel DLP-printed molds have also been demonstrated [30, 78]. However, these devices face the same limitations of PDMS microfluidic chips discussed in the Introduction. In this work, we successfully printed a test microfluidic chip with a straight channel featuring a nominal cross-section of 100 × 50 µm^2, with only a brief optimization of printing parameters (Fig. S5). Considering the nominal *X* and *Y* resolution of our 3D printer (Asiga MAX X27), printing a 100-µm-wide channel (equivalent to only 4 pixels) was a daunting task. Attempts to print smaller channels (e.g., a nominal cross-section of 75 × 50 µm^2) were unsuccessful due to unpredictable channel blockages caused by the limited fidelity of the projection optics, consistent with findings from previous studies using similar DLP systems [74]. Using our proposed fabrication technique, we achieved a microchannel with a cross-section of 76.1 × 50.9 µm^2 (Fig. 7), which is just a single pixel narrower than the nominal 100-µm-wide design. This represents a significant improvement over prior work, where the smallest cross-section achieved with a commercial printer (Asiga PICO Plus 27) and a custom resin was 108 × 60 µm^2 [74]. Moreover, our hybrid chip exhibited superior optical quality compared to this monolithically 3D-printed chip.

The reduction in the cross-sectional area of the smallest channel, compared to the 3D-printed original (90.6 × 50.2 µm^2), was 14.8%, indicating that removing residual resins from smaller channels is more difficult (as evidenced by a 2.1% reduction for a larger channel with a cross-section of 173 × 102 µm^2 in Fig. 6a and a 6% reduction for a channel measuring 164.2 × 196.5 µm^2 in Fig. 9). Therefore, using a UV adhesive with lower viscosity could be essential in achieving sub-100-µm channels with better dimensional accuracy. Overall, our method of forming a narrow, enclosed microchannel using a commercial 3D printer and an off-the-shelf adhesive was both effective and practical.

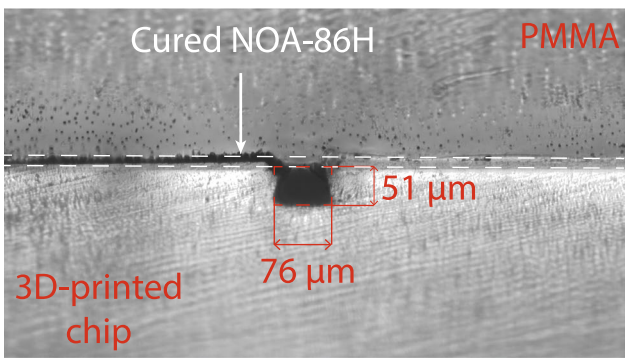

Fig. 7 A sub-100-µm microchannel shown in an optical micrograph. The nominal channel cross-section was 100 × 50 µm^2. The actual dimensions measured 90.6 × 50.2 µm^2 before bonding and 76.1 × 50.9 µm^2 after bonding

3.4 Bonding Strength Measurement

One of the most crucial properties of a bonded microfluidic device is its bonding strength, which is essential for preventing leakage under high flow-rate or high-pressure conditions. The burst opening method is adopted in this work because tensile and shear tests require prohibitively expensive and complex setups and do not directly apply to specific chip designs [47]. The goal was to compare different UV adhesives by measuring the burst pressure, thereby identifying the superior adhesive for use in fabricating functional microfluidic devices.

For the burst test, a straight-channel chip was designed and fabricated using NOA-86H and PR-48 adhesive. A crucial factor considered was the Ratio of the Bonded area to the overall Chip area (RBC) because burst strength increases with a higher RBC [65, 71]. Initially, we tested a chip with an RBC value of 0.977 (bonded area = 586.3 mm^2 and overall chip area = 600 mm^2). As anticipated, the chip demonstrated strong bonding. Leakage occurred prematurely through tube fittings and connections, but not through the bonded interface between the 3D-printed chip and the PMMA cover plate for both adhesives. Therefore, burst pressure could not be measured with our setup. To address this problem, the burst-test chip was redesigned with a reduced RBC value of 0.895 (bonded area = 536.86 mm^2 and overall chip area = 600 mm^2), allowing leakage to occur through the bonded interface. This redesign enabled successful measurement and comparison of burst strengths between the two adhesives.

The graphs in Fig. 8 show the pressure measured inside the two burst-test chips as a function of time. Owing to the compliance of the hydraulic network (i.e., deformation of tubes, chips, and fittings under pressure), pressure gradually increased over time upon flow injection, although the network was already filled with water. Eventually, the test chip burst as the pump increased pressure. For the chip bonded with PR-48, the same resin used for 3D printing the chip, the burst pressure was 754 kPa (at 29.5 s). Leakage occurred through the bonded interface, as evidenced by red smears and droplets. In contrast, the chip bonded with NOA-86H did not burst at this pressure. Instead, leakage did occur through the outlet Luer connection at 869 kPa (at 81.1 s). Therefore, the burst pressure of the chip bonded with NOA-86H must be larger than 869 kPa, although the exact value could not be measured due to persistent leakage through fittings and connections, despite several tightening attempts. For accurate measurement, metal fittings and connectors capable of withstanding larger pressure should be used. Based on these results, we concluded that NOA-86H is the overall superior adhesive, offering higher burst pressure and similar dimensional accuracy. Accordingly, NOA-86H was selected for the fabrication of two functional microfluidic devices (i.e., inertial focusing and droplet generation applications).

To contextualize the achieved bonding strength, we compared it with previously reported values in the literature (Table S2). Given the extensive research on this topic, we limited our comparison to studies that meet the following criteria: (1) bonding between a 3D-printed chip and a cover plate, and (2) cases where bonding methods, bonding-strength measurement techniques, and bonding strengths were clearly described. This comparison includes details such as 3D printing methods (e.g., DLP, FDM), measurement techniques (e.g., burst-leakage test, tensile test), cover-plate materials (e.g., PMMA, PDMS), and bonding methods (e.g., adhesive bonding, thermal bonding). However, direct comparisons are inherently challenging due to variations in measurement techniques and the ratio of bonded area to

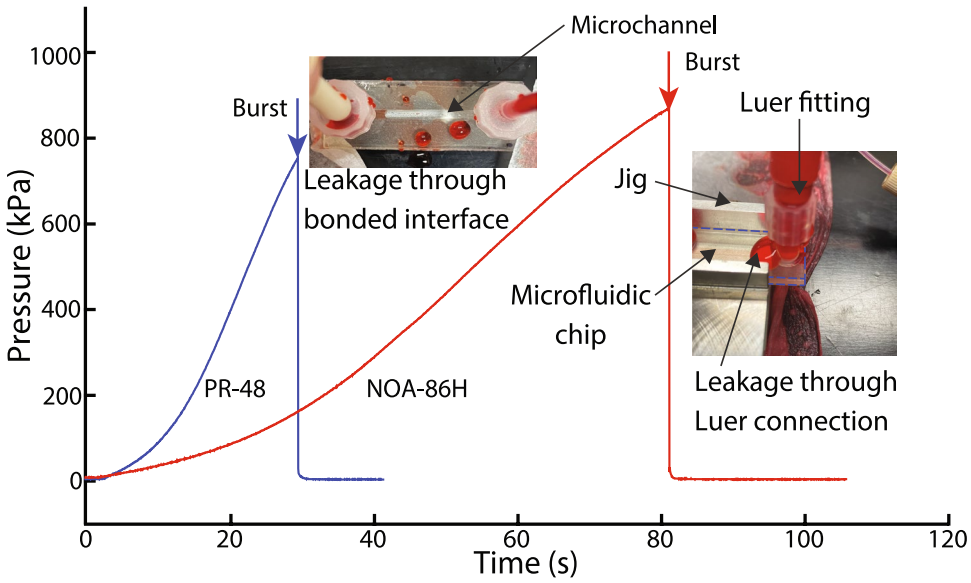

Fig. 8 Burst-test results. A test chip bonded using PR-48 burst at 754 kPa, with red food coloring leaking through the bonded interface between the PMMA cover plate and the 3D-printed chip. In contrast, the test chip bonded with NOA-86H did not burst even at 869 kPa. Instead, persistent leakage occurred through the outlet Luer connection despite multiple tightening attempts, suggesting that the actual burst pressure exceeds 869 kPa

overall chip area (RBC). The reported bonding strengths in the literature range from 71 to 1352 kPa [30, 43, 48, 49, 57, 79, 80]. Our bonding strength of > 869 kPa ranks among the top three highest reported values. The bonding strength between an adhesive-bonded (double-sided tape) PMMA and a DLP-printed chip was 1034 kPa [43]. However, Saffman–Taylor instability appeared at 570 kPa, indicating weakened bonding at this pressure and potential risk of channel deformation. The highest reported bonding strength (1352 kPa) was achieved using solvent bonding between an FDM-printed chip and a PMMA cover plate [48]. However, this measurement was conducted while the chip-cover plate assembly was mechanically clamped using an aluminum jig, suggesting the bonding strength could be overestimated. Overall, our bonding technique demonstrates excellent performance, ranking among the strongest bonding methods reported for hybrid 3D-printed microfluidic devices.

3.5 Microparticle Concentration Using Inertial Focusing

Inertial focusing is a fluidic phenomenon where suspended particles flowing at high velocities migrate across streamlines and form well-defined equilibrium positions in a transverse plane [81–83]. Over the past two decades, microfluidic inertial focusing has been extensively studied due to its ability to manipulate bioparticles, including fungi, bacteria, viruses, blood cells, and exosomes, at high throughput [82, 84, 85]. Unlike active microparticle manipulation methods, which require external energy source or force fields, inertial focusing can be implemented in a relatively straightforward manner; pushing particles through microfluidic channels with special geometries such as asymmetric curves, spirals, or expansion–contraction arrays would be sufficient for focusing particles when fluidic and geometrical conditions are met [86]. Highlighted applications include sheathless particle alignment (e.g., flow cytometry), particle filtration and separation (e.g., wastewater purification, blood plasma extraction, circulating tumor cell enrichment), solution exchange (e.g., colorimetric cell staining), microfiber fabrication (e.g., polymeric fiber with non-circular cross-sections), and hydrodynamic cell phenotyping (e.g., deformability-based cell classification) [87].

Inertial focusing operates within an intermediate Reynolds number range (~ 1 < Re < ~ 100), characterized by higher flow velocities compared to the conventional microfluidic regime where fluid inertia is negligible (Re ≪ 1). In this flow regime, both fluid inertia and viscosity are non-negligible, resulting in inertial fluidic effects such as the wall lift-force F_{LW} and shear-gradient lift force F_{SG} that act on particles to migrate to equilibrium positions. The number of equilibrium positions can be reduced by the Dean drag force F_D caused by secondary flow drag in curved channels, leading to a single focused particle stream [86]. Pressure can be significant in this flow regime and may deform flexible substrates like PDMS. This change of the channel shape may disturb focusing conditions, leading to poor or unpredictable performance. Therefore, rigid substrate materials such as PMMA, COC, or PC are generally preferred [43, 82]. Of course, bonding strength becomes a critical factor under these high flow-rate and high-pressure conditions, making our fabrication method ideal for manufacturing inertial microfluidic devices. A similar fabrication approach was previously made with tape adhesives [43, 88]. However, the bonding of a 3D-printed chip and PMMA using a pressure-sensitive adhesive tape may result in particle adsorption to exposed adhesive surfaces and cover-plate debonding at high flow rates [43].

Based on the device design (Fig. 3), the ratio between particle size a and hydraulic diameter D_h, a/D_h, is calculated to be 0.2, which is greater than the critical value of 0.07 required for inertial focusing to be achieved [86]. The ratio of shear-gradient lift force (F_{SG}) to the Dean drag force (F_D), denoted as R_f, is given by the equation:

$$R_f = \frac{a^2 R}{h^3}, \tag{1}$$

where R represents the radius of curvature of a curved segment, and h is the smallest channel dimension. For our design, R_f is calculated to be 0.128, which exceeds the threshold value of 0.04, thereby ensuring focusing at a single equilibrium position [82, 83, 89].

We assessed the fabrication accuracy by examining the channel cross-sections before and after bonding at two locations: the widest part of a curved segment (Fig. 9a) and the imaging section (Fig. 9b). The channel dimensions were characterized using the laser profilometer VK-X3000 before bonding and then using a BX-40 microscope after bonding, following the method described in Sect. 2.4. The results indicated a minimal reduction in-channel cross-section, only 3% for the curved segment and 6% for the imaging section, reaffirming the excellent precision of our bonding technique.

The operational condition (i.e., flow rate) was estimated using dimensionless-number analyses. The channel Reynolds number (Re_c) is defined as:

$$Re_c = \frac{\rho U D_h}{\eta}, \tag{2}$$

where ρ is the fluid density, U is the flow velocity, and η is the dynamic viscosity. At a flow rate of 100 µl/min (flow velocity = 41.7 mm/s), Re_c is 9.29, placing the flow between the Stoke regime and turbulent regime [87]. The particle Reynolds number (Re_p) is defined as:

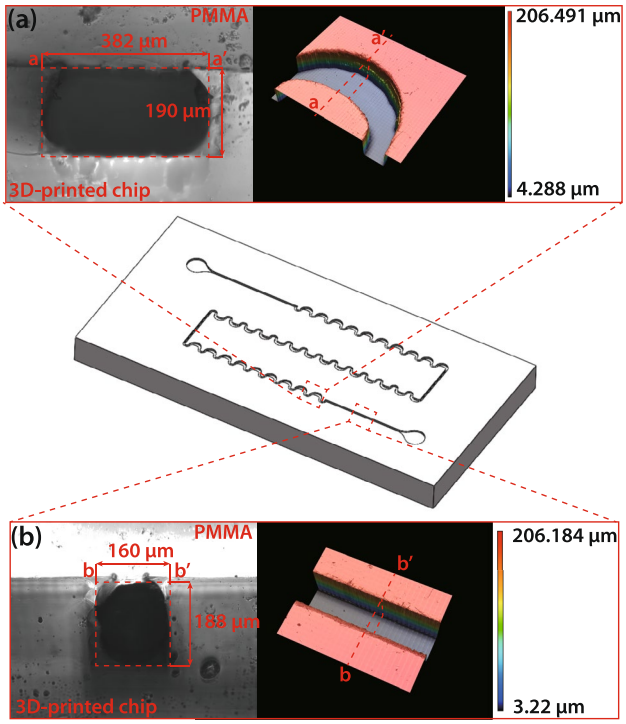

Fig. 9 Inertial focusing device fabricated to demonstrate our bonding technique. The fabrication quality was assessed by comparing cross-sections before and after bonding. The channel cross-sections were reduced by only 3% in the curved segment and 6% in the straight section, underscoring the precision of our technique

$$\mathrm{Re_p} = \mathrm{Re_c}\left(\frac{a}{D_h}\right)^2. \tag{3}$$

In our case, $\mathrm{Re_p}$ is 0.371, approaching the condition $\mathrm{Re_p}\approx 1$ required for inertial focusing [83]. The Dean number, which reflects the strength of the secondary flow in the curved channel, is defined as:

$$\mathrm{De} = \mathrm{Re_c}\sqrt{\frac{D_h}{2R}}.$$

The calculated Dean number is 3.67. These dimensionless parameters, $\mathrm{De} = 3.67$ and $a/D_h = 0.2$, confirm that our device with asymmetrically curved segments operates under appropriate inertial-focusing conditions, consistent with the phase diagram published by Di Carlo [86]. In addition, these dimensionless parameters are similar to those reported in prior studies of inertial focusing in curved or spiral channel designs [83]. Consequently, we selected a flow rate of 100 µl/min for the inertial focusing experiments.

Progressive focusing of particles into a single stream is observed downstream. As shown in the fluorescence streamline images in Fig. 10, the beads were initially unfocused, spanning nearly the entire channel width in the inlet section

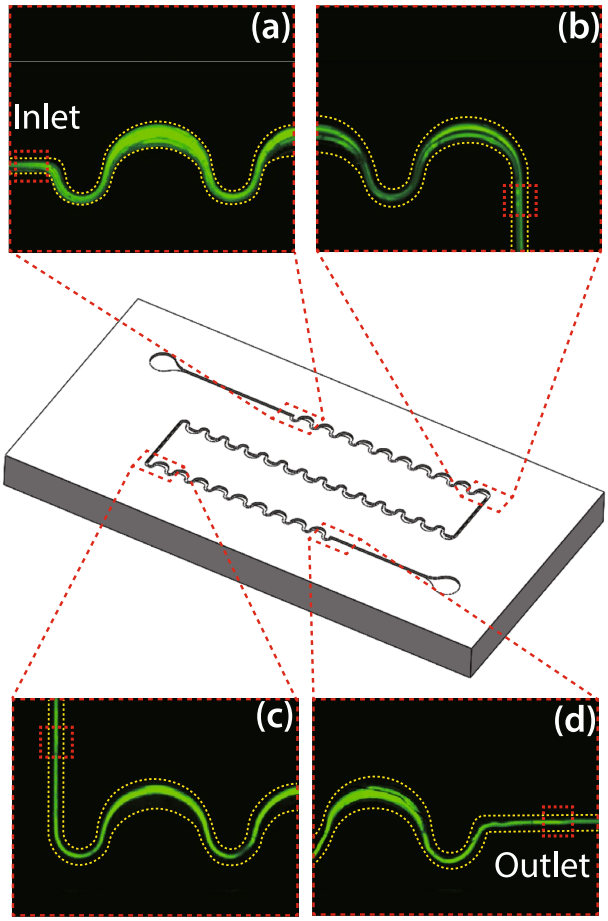

Fig. 10 Inertial focusing result. Fluorescence microbeads (40 µm) are progressively focused from **a** the inlet (150.3 µm), **b** after the 10th curved segment (95.6 µm), **c** before the 25th curved segment (49.5 µm), and **d** at the outlet imaging Sect. (50.8 µm). The width of the final streamline is equivalent to 1.27 times the bead diameter, indicating that inertial focusing is completed. The regions where width measurements are taken are marked with red-dotted boxes

(150.3 µm, Fig. 10a). However, they gradually became focused: 95.6 µm after the 10th segment (Fig. 10b), 49.5 µm before the 25th segment (Fig. 10c), and 50.8 µm after the last segment (Fig. 10d). The streamline width in the imaging section was less than twice the particle diameter (1.27×), indicating that inertial focusing was achieved [89]. Notably, focusing was already accomplished just before the 25th segment, where the streamline width was equivalent to 1.23 times the bead diameter. The streamline images also demonstrate the superior optical transparency of our fabricated device for fluorescence imaging.

The pressure at this high flow rate was measured using an in-line pressure sensor EIPS345 (Fluigent), which has a smaller measurement range (138 vs. 1379 kPa) but higher resolution (0.14 vs. 1.38 kPa) compared to the sensor used for the burst test. The pressure was recorded at 2.45 kPa (Fig. S6), lower than the observed burst strength

(> 869 kPa). In addition, the ratio of bonded area to the overall chip area (RBC) of the inertial focusing chip was 0.995 (bonded area = 764.3 mm^2 and overall chip area = 768 mm^2), indicating stronger adhesion compared to the burst-test chip (RBC = 0.977). Consequently, no leakage was observed in the inertial focusing chip. Given that our devices can sustain more than 869 kPa, we anticipate that this fabrication method will be suitable for inertial focusing devices operating under more demanding conditions because Reynolds numbers can be up to 100 times larger in many inertial focusing applications, potentially resulting in significantly higher pressure [82, 83, 89]. Although we were unable to test such high flow rates due to the performance limitation of our syringe pump in hand, we plan to explore these demanding conditions in future studies. In summary, a well-performing microfluidic particle-focusing device was produced using our fabrication technique.

3.6 Microfluidic Water-in-Oil Droplet Generation

In the second demonstration, a microfluidic droplet generator was fabricated and evaluated (Fig. 11a). Droplet microfluidics enables the generation, manipulation, modification, and quantification of discrete micro- and nanoscale droplets and particles. Monodisperse, evenly spaced droplets can be produced in a continuous stream with high throughput [90]. Compared to bulk emulsification methods, droplet microfluidics offers precise control of droplet size and morphology, size distribution, and encapsulated substance composition [91]. Since its inception, droplet microfluidics has expanded rapidly beyond a simple emulsification and particle synthesis into biomedical applications, including biomolecular analysis (e.g., nucleic acids, protein, enzyme), cell biology (e.g., cellular interactions, artificial cell generation), diagnostics (e.g., microbial infections, oncology assays, genetic mutations), drug development (drug delivery systems, drug screening platforms), and tissue engineering [91].

For droplet generation, the injected dispersed-phase fluid (i.e., reagents and samples) and continuous-phase fluid (i.e., carrier fluid) join at a junction, forming an immiscible interface. The viscous drag exerted by the continuous phase on the dispersed phase overcomes the interfacial tension, elongates the interface with a large deformation, and eventually destabilizes the interface [91, 92]. This unstable interface fragments spontaneously (i.e., shedding the dispersed phase), producing a stream of discrete droplets. The Capillary number (Ca), a dimensionless number representing the ratio of viscous stress to capillary pressure, characterizes the droplet generation regime, namely squeezing, dripping, jetting, tip-streaming, and tip-multi-breaking regimes [92]:

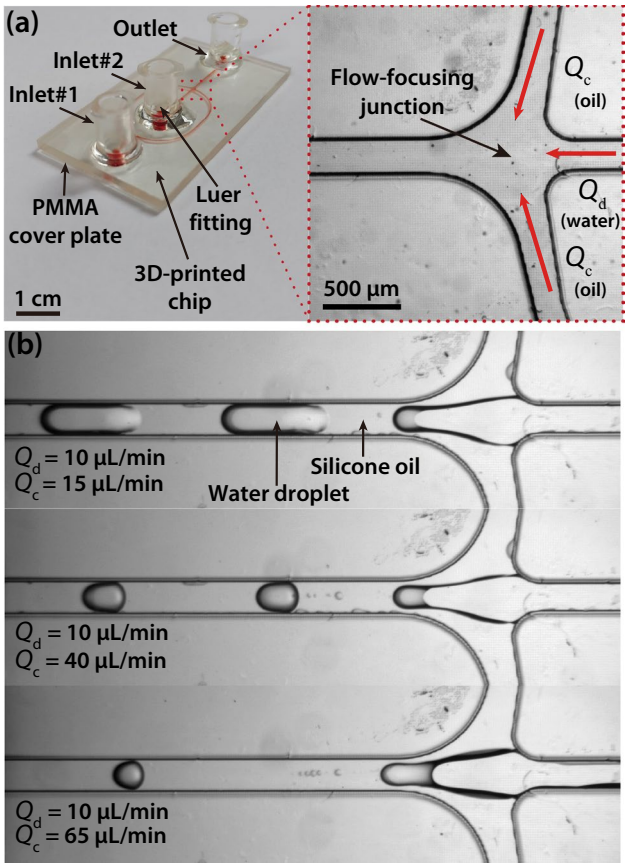

Fig. 11 **a** A photograph of the fabricated droplet generator chip. The inset figure highlights the junction where two slanted, counter-streaming channels for the oil phase intersect with the horizontal channel for the water phase. The flow rates for the continuous phase (silicone oil) and dispersed phase (DI water) are denoted as Q_c and Q_d, respectively. **b** Operation of the droplet generator. Q_d is fixed at 10 µl/min, while Q_c is varied: 15, 40, and 64 µl/min. As Q_c increases, the shear stress increases, resulting in a decrease in water-in-oil droplet size due to the more rapid fragmentation of the dispersed phase

$$\mathrm{Ca} = \frac{\eta U}{\gamma}, \tag{4}$$

where η is the dynamic viscosity, and γ is the interfacial tension. Typically, Ca value ranges from 10^{-3} to 10^{1}. Another important parameter is φ the ratio of the flow rates of the dispersed phase to the continuous phase:

$$\varphi = \frac{Q_d}{Q_c}, \tag{5}$$

where Q_d and Q_c are the flow rates for the dispersed and continuous phases, respectively (Fig. 11b).

The flow rate for the DI water (Q_d) was fixed at 10 µl/min, while the flow rate for the silicone oil (Q_c), which has higher density and viscosity than those of DI water, was varied at 15, 40, and 65 µl/min. At these flow rates,

the channel Reynolds number Re_c ranged from 0.008 to 0.0347, indicating that droplet generation occurred in the laminar-flow regime. The capillary number for the continuous phase (Ca_c) was calculated to be between 0.0118 and 0.0511 (with dynamic viscosity $\eta = 0.0962$ Pa s, surface tension $\gamma = 2.09 \times 10^{-2}$ N/m, and flow velocity $U = 2.56 \times 10^{-3} \sim 1.111 \times 10^{-2}$ m/s). The volume flow rate ratio φ ranged from 1.5 to 6.5. Under these operating conditions, the droplet generation is classified as the "squeezing" regime, which is suitable for producing monodisperse droplets as shown in Fig. 11b [91, 92]. The squeezing regime is characterized by the dispersed phase protruding into the outlet channel and producing droplets larger than the outlet-channel width [92]. As φ (or Q_c) increases, shear stress increases, causing the water stream to break more rapidly and generating smaller droplets. The droplet length L_p measured 1121, 451, and 327 µm for Q_c values of 15, 40, and 65 µl/min, respectively (Fig. 11b). As expected, the droplet size can be controlled by adjusting the flow rate. Further reduction of droplet size (e.g., < 100 µm) can be achieved by narrowing the inlet-channel width for the dispersed phase (i.e., orifice width) or further increasing φ [93, 94]. Using the same chip, we achieved 98.3-µm droplets by increasing φ (Fig. S7).

The images of monodisperse droplets also demonstrate the superior optical transparency of our fabricated device for brightfield imaging. No leakage was observed in the chip, which was expected given the lower flow velocity compared to the inertial focusing device (11.1 vs. 41.7 mm/s). This result further verifies the effectiveness of our fabrication method in prototyping droplet microfluidic devices in terms of imaging and device robustness.

4 Conclusion

DLP-3D printing has emerged as an excellent alternative to PDMS for prototyping microfluidic devices, offering the ability to fabricate arbitrary 3D shapes with suitable precision and speed, directly from a CAD design without the need for a cleanroom, expensive photolithographic equipment, or highly skilled personnel. A critical limitation of DLP printing, however, has been the translucent nature of the printed material, which impedes its broader adoption. To overcome this limitation, diverting from previous time- and labor-intensive surface-treatment methods, we proposed a practical and effective method for prototyping microfluidic devices with enhanced optical transparency through the adhesive bonding of a PMMA cover plate to a DLP-printed open-channel microfluidic chip. A key innovation in our fabrication technique was the use of vacuum suction to remove liquid adhesive from microchannels in a temporarily bonded device, followed by UV adhesive curing. NOA-86H was selected due to its optical transparency, strong adhesion between plastics, and higher burst strength compared to PR-48. The relatively low viscosity (250–350 cps) of NOA-86H was particularly advantageous in removing residual adhesive from microchannel networks.

The optical transparency of the hybrid PMMA-DLP print device is significantly superior to that of a conventional, monolithically 3D-printed device, making it suitable for optical detection and microscopic observation applications. In addition, the device demonstrated notable burst strength exceeding 869 kPa, which gauges resistance to pressure in a microfluidic network. This burst strength seems sufficient for most microfluidic applications. Dimensional variation was limited to 2.1% for the channel with a cross-section of 173 × 102 µm^2, which is a marked improvement over a similar previous study where channel widths smaller than 250 µm were completely occluded. Printing of sub-100-µm microchannels with a typical aspect ratio using a commercial DLP printer and off-the-shelf resins has been particularly challenging due to difficulties in removing uncured resins infiltrated into the channels. However, we achieved the smallest channel cross-section of 76.1 × 50.9 µm^2, a notable improvement from the previous work using either a similar bonding technique (250 × 250 µm^2) or monolithic DLP printing (180 × 60 µm^2). Given that these small microchannels were fabricated simply and successfully using a commercial DLP printer and resin, we anticipate broad adoption of our fabrication method in biology and biochemistry labs often lacking engineering expertise.

As a proof of concept, we fabricated functional microfluidic devices for two major applications: inertial focusing and droplet generation. The inertial focusing devices effectively enriched and aligned dispersed 40-µm fluorescence microbeads at a high flow rate of 100 µL/min. The droplet generator produced a continuous stream of water-in-oil droplets ranging from 98 to 1121 µm in size at high throughputs. Both devices exhibited excellent optical transparency as intended, which was demonstrated by fluorescent traces of flowing beads and brightfield images of migraing monodisperse droplets. The versatility of our fabrication method was further highlighted by fabricating the two devices in different orientations: one with a conventional orientation, the 3D-printed chip on the bottom and the PMMA cover plate on top, and the other with the opposite orientation, the chip on top and the cover plate on the bottom. The overall fabrication time from chip printing to bonding was only 1–2 h, depending primarily on a printing parameter (e.g., layer thickness) and the channel complexity (i.e., vacuum suction).

Our approach may limit the design flexibility of 3D-device architectures (e.g., a spiral microchannel with trapezoid cross-section for size-selective separation of bacterial cells [95], a DNA-inspired microfluidic system

architecture [96], and a 3D micromixer [18]) because at least one side of the device should be planar for bonding to a flat PMMA substrate. However, this can be mitigated by designing devices with a single or few planar regions to serve as a transparent window for optical quantification or analysis, while the remaining structure can fully harness the advantages of 3D microfluidic architectures [35].

We are currently exploring methods to accurately measure burst strength using metallic fittings and connections while also expanding our bonding technique to include other transparent substrates such as PC, COC, PS, and glass. In addition, we are refining our bonding approach to develop a sheathless cell-focusing device for image flow cytometry-based cell identification [97], recognizing the potential of our technology in developing high-performance inertial focusing methods. We anticipate our hybrid bonding technique will facilitate the widespread adoption of 3D-printed microfluidic device prototyping across various fields and disciplines.

Supplementary Information The online version contains supplementary material available at https://doi.org/10.1007/s13206-025-00206-1.

Acknowledgements This work was supported by 2024 Research Fund of Myongji University.

Data availability Not applicable

Declarations

Conflict of interest The authors declare that they have no conflict of interest.

References

1. Sackmann, E.K., Fulton, A.L., Beebe, D.J.: The present and future role of microfluidics in biomedical research. Nature **507**, 181–189 (2014). https://doi.org/10.1038/nature13118
2. Duncombe, T.A., Tentori, A.M., Herr, A.E.: Microfluidics: reframing biological enquiry. Nat. Rev. Mol. Cell Biol. **16**, 554–567 (2015). https://doi.org/10.1038/nrm4041
3. Ren, K., Zhou, J., Wu, H.: Materials for microfluidic chip fabrication. Acc. Chem. Res. **46**, 2396–2406 (2013). https://doi.org/10.1021/ar300314s
4. Tang, T., Yuan, Y., Yalikun, Y., Hosokawa, Y., Li, M., Tanaka, Y.: Glass based micro total analysis systems: materials, fabrication methods, and applications. Sens. Actuators B Chem. **339**, 129859 (2021). https://doi.org/10.1016/j.snb.2021.129859
5. Kim, J., Kim, S.-I., Joung, Y.-H., Choi, J., Koo, C.: Two-step hybrid process of movable part inside glass substrate using ultrafast laser. Micro Nano Syst. Lett. **9**, 16 (2021). https://doi.org/10.1186/s40486-021-00142-3
6. Sia, S.K., Whitesides, G.M.: Microfluidic devices fabricated in poly(dimethylsiloxane) for biological studies. Electrophoresis **24**, 3563–3576 (2003). https://doi.org/10.1002/elps.200305584
7. Bhattacharjee, N., Urrios, A., Kang, S., Folch, A.: The upcoming 3D-printing revolution in microfluidics. Lab Chip **16**, 1720–1742 (2016). https://doi.org/10.1039/C6LC00163G
8. Namgung, H., Kaba, A.M., Oh, H., Jeon, H., Yoon, J., Lee, H., Kim, D.: Quantitative determination of 3D-printing and surface-treatment conditions for direct-printed microfluidic devices. Biochip J. **16**, 82–98 (2022). https://doi.org/10.1007/s13206-022-00048-1
9. Jeon, H., Mirgissa, K.A., Baek, S., Rhee, K., Kim, D.: Excitation-frequency determination based on electromechanical impedance spectroscopy for a laser-microfabricated cavitation microstreaming micromixer. Sens. Actuators A Phys. **326**, 112730 (2021). https://doi.org/10.1016/j.sna.2021.112730
10. Jung, D., Jang, S., Park, D., Bae, N.H., Han, C.S., Ryu, S., Lim, E.-K., Lee, K.G.: Automated microfluidic systems facilitating the scalable and reliable production of lipid nanoparticles for gene delivery. Biochip J. (2024). https://doi.org/10.1007/s13206-024-00182-y
11. Young, E.W.K., Berthier, E., Guckenberger, D.J., Sackmann, E., Lamers, C., Meyvantsson, I., Huttenlocher, A., Beebe, D.J.: Rapid prototyping of arrayed microfluidic systems in polystyrene for cell-based assays. Anal. Chem. **83**, 1408–1417 (2011). https://doi.org/10.1021/ac102897h
12. Kaba, A.M., Jeon, H., Park, A., Yi, K., Baek, S., Park, A., Kim, D.: Cavitation-microstreaming-based lysis and DNA extraction using a laser-machined polycarbonate microfluidic chip. Sens. Actuators B Chem. **346**, 130511 (2021). https://doi.org/10.1016/j.snb.2021.130511
13. Kim, S., Lee, J.-B., Kim, D., Kim, K., Sung, G.Y.: Fabrication of nephrotoxic model by kidney-on-a-chip implementing renal proximal tubular function in vitro. Biochip J. **18**, 477–484 (2024). https://doi.org/10.1007/s13206-024-00166-y
14. Riegger, L., Strohmeier, O., Faltin, B., Zengerle, R., Koltay, P.: Adhesive bonding of microfluidic chips: influence of process parameters. J. Micromech. Microeng. **20**, 087003 (2010). https://doi.org/10.1088/0960-1317/20/8/087003
15. Lee, W., Yoon, B., Lee, J., Jung, S., Oh, Y.S., Ko, J., Jeon, N.L.: Machine learning-aided three-dimensional morphological quantification of angiogenic vasculature in the multiculture microfluidic platform. Biochip J. **17**, 357–368 (2023). https://doi.org/10.1007/s13206-023-00114-2
16. Chin, C.D., Linder, V., Sia, S.K.: Commercialization of microfluidic point-of-care diagnostic devices. Lab Chip **12**, 2118–2134 (2012). https://doi.org/10.1039/C2LC21204H
17. Au, A.K., Huynh, W., Horowitz, L.F., Folch, A.: 3D-printed microfluidics. Angew. Chem. Int. Ed. **55**, 3862–3881 (2016). https://doi.org/10.1002/anie.201504382
18. Waheed, S., Cabot, J.M., Macdonald, N.P., Lewis, T., Guijt, R.M., Paull, B., Breadmore, M.C.: 3D printed microfluidic devices: enablers and barriers. Lab Chip **16**, 1993–2013 (2016). https://doi.org/10.1039/C6LC00284F
19. Amin, R., Knowlton, S., Hart, A., Yenilmez, B., Ghaderinezhad, F., Katebifar, S., Messina, M., Khademhosseini, A., Tasoglu, S.: 3D-printed microfluidic devices. Biofabrication **8**, 022001 (2016). https://doi.org/10.1088/1758-5090/8/2/022001
20. Naderi, A., Bhattacharjee, N., Folch, A.: Digital manufacturing for microfluidics. Annu. Rev. Biomed. Eng. **21**, 325–364 (2019). https://doi.org/10.1146/annurev-bioeng-092618-020341
21. Nielsen, A.V., Beauchamp, M.J., Nordin, G.P., Woolley, A.T.: 3D printed microfluidics. Annu. Rev. Anal. Chem. **13**, 45–65 (2020). https://doi.org/10.1146/annurev-anchem-091619-102649
22. Capel, A.J., Rimington, R.P., Lewis, M.P., Christie, S.D.R.: 3D printing for chemical, pharmaceutical and biological applications. Nat. Rev. Chem. **2**, 422–436 (2018). https://doi.org/10.1038/s41570-018-0058-y
23. Yazdi, A.A., Popma, A., Wong, W., Nguyen, T., Pan, Y., Xu, J.: 3D printing: an emerging tool for novel microfluidics and lab-on-a-chip applications. Microfluid. Nanofluid. **20**, 50 (2016). https://doi.org/10.1007/s10404-016-1715-4

24. Amini, A., Guijt, R.M., Themelis, T., De Vos, J., Eeltink, S.: Recent developments in digital light processing 3D-printing techniques for microfluidic analytical devices. J. Chromatogr. A **1692**, 463842 (2023). https://doi.org/10.1016/j.chroma.2023.463842
25. Gonzalez, G., Roppolo, I., Pirri, C.F., Chiappone, A.: Current and emerging trends in polymeric 3D printed microfluidic devices. Addit. Manuf. **55**, 102867 (2022). https://doi.org/10.1016/j.addma.2022.102867
26. Fritschen, A., Bell, A.K., Königstein, I., Stühn, L., Stark, R.W., Blaeser, A.: Investigation and comparison of resin materials in transparent DLP-printing for application in cell culture and organs-on-a-chip. Biomater. Sci. **10**, 1981–1994 (2022). https://doi.org/10.1039/D1BM01794B
27. Beckwith, A.L., Borenstein, J.T., Velásquez-García, L.F.: Monolithic, 3D-printed microfluidic platform for recapitulation of dynamic tumor microenvironments. J. Microelectromech. Syst. **27**, 1009–1022 (2018). https://doi.org/10.1109/JMEMS.2018.2869327
28. Urrios, A., Parra-Cabrera, C., Bhattacharjee, N., Gonzalez-Suarez, A.M., Rigat-Brugarolas, L.G., Nallapatti, U., Samitier, J., DeForest, C.A., Posas, F., Garcia-Cordero, J.L., Folch, A.: 3D-printing of transparent bio-microfluidic devices in PEG-DA. Lab Chip **16**, 2287–2294 (2016). https://doi.org/10.1039/C6LC00153J
29. Bhattacharjee, N., Parra-Cabrera, C., Kim, Y.T., Kuo, A.P., Folch, A.: Desktop-stereolithography 3D-printing of a poly(dimethylsiloxane)-based material with sylgard-184 properties. Adv. Mater. **30**, 1800001 (2018). https://doi.org/10.1002/adma.201800001
30. Kecili, S., Tekin, H.C.: Adhesive bonding strategies to fabricate high-strength and transparent 3D printed microfluidic device. Biomicrofluidics **14**, 024113 (2020). https://doi.org/10.1063/5.0003302
31. He, Y., Xue, G.-H., Fu, J.-Z.: Fabrication of low cost soft tissue prostheses with the desktop 3D printer. Sci. Rep. **4**, 6973 (2014). https://doi.org/10.1038/srep06973
32. Gross, B.C., Anderson, K.B., Meisel, J.E., McNitt, M.I., Spence, D.M.: Polymer coatings in 3D-printed fluidic device channels for improved cellular adherence prior to electrical lysis. Anal. Chem. **87**, 6335–6341 (2015). https://doi.org/10.1021/acs.analchem.5b01202
33. https://formlabs.com/kr/blog/3d-printing-transparent-parts-techniques-for-finishing-clear-resin/. Accessed 16 Aug 2024.
34. Zips, S., Wenzel, O.J., Rinklin, P., Grob, L., Terkan, K., Adly, N.Y., Weiß, L., Wolfrum, B.: Direct stereolithographic 3D printing of microfluidic structures on polymer substrates for printed electronics. Adv. Mater. Technol. **4**, 1800455 (2019). https://doi.org/10.1002/admt.201800455
35. Bressan, L.P., Adamo, C.B., Quero, R.F., de Jesus, D.P., da Silva, J.A.F.: A simple procedure to produce FDM-based 3D-printed microfluidic devices with an integrated PMMA optical window. Anal. Methods **11**, 1014–1020 (2019). https://doi.org/10.1039/C8AY02092B
36. Gaal, G., Mendes, M., de Almeida, T.P., Piazzetta, M.H.O., Gobbi, Â.L., Riul, A., Rodrigues, V.: Simplified fabrication of integrated microfluidic devices using fused deposition modeling 3D printing. Sens. Actuators B Chem. **242**, 35–40 (2017). https://doi.org/10.1016/j.snb.2016.10.110
37. de Bruin, A., Friddin, M.S., Elani, Y., Brooks, N.J., Law, R.V., Seddon, J.M., Ces, O.: A transparent 3D printed device for assembling droplet hydrogel bilayers (DHBs). RSC Adv. **7**, 47796–47800 (2017). https://doi.org/10.1039/C7RA09406J
38. Ergin, F.G., Watz, B.B., Gade-Nielsen, N.F.: A review of planar PIV systems and image processing tools for lab-on-chip microfluidics. Sensors **18**, 3090 (2018). https://doi.org/10.3390/s18093090
39. Arega, N.G., Heard, W.N., Tran, N.A.N., Jung, S., Meng, J., Chung, M., Kim, M.-S., Kim, D.: Zinc-finger-protein-based microfluidic electrophoretic mobility reversal assay for quantitative double-stranded DNA analysis. Biochip J. **15**, 381–395 (2021). https://doi.org/10.1007/s13206-021-00038-9
40. Su, R., Wang, F., McAlpine, M.C.: 3D printed microfluidics: advances in strategies, integration, and applications. Lab Chip **23**, 1279–1299 (2023). https://doi.org/10.1039/D2LC01177H
41. Bishop, G.W.: 3D printed microfluidic devices. In: Dixit, C.K., Kaushik, A. (eds.) Microfluidics for Biologists: Fundamentals and Applications, pp. 103–113. Springer International Publishing, Cham (2016)
42. van der Linden, P.J.E.M., Popov, A.M., Pontoni, D.: Accurate and rapid 3D printing of microfluidic devices using wavelength selection on a DLP printer. Lab Chip **20**, 4128–4140 (2020). https://doi.org/10.1039/D0LC00767F
43. Razavi Bazaz, S., Rouhi, O., Raoufi, M.A., Ejeian, F., Asadnia, M., Jin, D.E., Warkiani, M.: 3D printing of inertial microfluidic devices. Sci. Rep. **10**, 5929 (2020). https://doi.org/10.1038/s41598-020-62569-9
44. Giri, K., Tsao, C.-W.: Recent advances in thermoplastic microfluidic bonding. Micromachines **13**, 486 (2022). https://doi.org/10.3390/mi13030486
45. Tsao, C.-W., DeVoe, D.L.: Bonding of thermoplastic polymer microfluidics. Microfluid. Nanofluid. **6**, 1–16 (2009). https://doi.org/10.1007/s10404-008-0361-x
46. Shakeri, A., Khan, S., Jarad, N.A., Didar, T.F.: The fabrication and bonding of thermoplastic microfluidics: a review. Materials **15**, 6478 (2022). https://doi.org/10.3390/ma15186478
47. Lu, Y., Ma, L., Chen, L., Wan, P., Fan, Y.: Review on bonding strength testing methods for polymer-based microfluidics. J. Adhes. Sci. Technol. (2024). https://doi.org/10.1080/01694243.2024.2358049
48. Lynh, H.D., Pin-Chuan, C.: Novel solvent bonding method for creation of a three-dimensional, non-planar, hybrid PLA/PMMA microfluidic chip. Sens. Actuators A Phys. **280**, 350–358 (2018). https://doi.org/10.1016/j.sna.2018.08.002
49. Duong, L.H., Chen, P.-C.: Simple and low-cost production of hybrid 3D-printed microfluidic devices. Biomicrofluidics (2019). https://doi.org/10.1063/1.5092529
50. Kim, D., Herr, A.E.: Protein immobilization techniques for microfluidic assays. Biomicrofluidics **7**, 041501 (2013). https://doi.org/10.1063/1.4816934
51. Ebnesajjad, S.: 8 — Characteristics of adhesive materials. In: Ebnesajjad, S. (ed.) Handbook of Adhesives and Surface Preparation, pp. 137–183. William Andrew Publishing, Oxford (2011)
52. Wu, H., Huang, B., Zare, R.N.: Construction of microfluidic chips using polydimethylsiloxane for adhesive bonding. Lab Chip **5**, 1393–1398 (2005). https://doi.org/10.1039/B510494G
53. Flachsbart, B.R., Wong, K., Iannacone, J.M., Abante, E.N., Vlach, R.L., Rauchfuss, P.A., Bohn, P.W., Sweedler, J.V., Shannon, M.A.: Design and fabrication of a multilayered polymer microfluidic chip with nanofluidic interconnects via adhesive contact printing. Lab Chip **6**, 667–674 (2006). https://doi.org/10.1039/B514300D
54. Tan, H.Y., Loke, W.K., Nguyen, N.-T.: A reliable method for bonding polydimethylsiloxane (PDMS) to polymethylmethacrylate (PMMA) and its application in micropumps. Sens. Actuators B Chem. **151**, 133–139 (2010). https://doi.org/10.1016/j.snb.2010.09.035
55. Huyen, L.T.N., Hong, S.J., Trung, T.Q., Meeseepong, M., Kim, A.R., Lee, N.-E.: Flexible capillary microfluidic devices based on surface-energy modified polydimethylsiloxane and polymethylmethacrylate with room-temperature chemical bonding. Biochip J. (2023). https://doi.org/10.1007/s13206-023-00096-1
56. Wang, S., Yu, S., Lu, M., Zuo, L.: Microfabrication of plastic-PDMS microfluidic devices using polyimide release layer

and selective adhesive bonding. J. Micromech. Microeng. **27**, 055015 (2017). https://doi.org/10.1088/1361-6439/aa66ed
57. Cheon, J., Kim, S.: Intermediate layer-based bonding techniques for polydimethylsiloxane/digital light processing 3D-printed microfluidic devices. J. Micromech. Microeng. **29**, 095005 (2019). https://doi.org/10.1088/1361-6439/ab27d3
58. Li, X., Wu, N., Rojanasakul, Y., Liu, Y.: Selective stamp bonding of PDMS microfluidic devices to polymer substrates for biological applications. Sens. Actuators A Phys. **193**, 186–192 (2013). https://doi.org/10.1016/j.sna.2012.12.037
59. Kim, H., Hwang, H., Baek, S., Kim, D.: Design, fabrication and performance evaluation of a printed-circuit-board microfluidic electrolytic pump for lab-on-a-chip devices. Sens. Actuators A Phys. **277**, 73–84 (2018). https://doi.org/10.1016/j.sna.2018.04.042
60. Baek, S., Kim, H., Hwang, H., Kaba, A.M., Kim, H., Chung, M., Kim, J., Kim, D.: A laser-micromachined PCB electrolytic micropump using an oil-based electrolyte separation barrier. Biochip J. **17**, 244–262 (2023). https://doi.org/10.1007/s13206-023-00100-8
61. Aladese, A.D., Jeong, H.-H.: Recent developments in 3D printing of droplet-based microfluidics. Biochip J. **15**, 313–333 (2021). https://doi.org/10.1007/s13206-021-00032-1
62. Chen, P.-C., Liu, Y.-M., Chou, H.-C.: An adhesive bonding method with microfabricating micro pillars to prevent clogging in a microchannel. J. Micromech. Microeng. **26**, 045003 (2016). https://doi.org/10.1088/0960-1317/26/4/045003
63. Carroll, S., Crain, M.M., Naber, J.F., Keynton, R.S., Walsh, K.M., Baldwin, R.P.: Room temperature UV adhesive bonding of CE devices. Lab Chip **8**, 1564–1569 (2008). https://doi.org/10.1039/B805554H
64. Dang, F., Shinohara, S., Tabata, O., Yamaoka, Y., Kurokawa, M., Shinohara, Y., Ishikawa, M., Baba, Y.: Replica multichannel polymer chips with a network of sacrificial channels sealed by adhesive printing method. Lab Chip **5**, 472–478 (2005). https://doi.org/10.1039/B417398H
65. Ku, X., Zhuang, G., Li, G.: A universal approach for irreversible bonding of rigid substrate-based microfluidic devices at room temperature. Microfluid. Nanofluid. **22**, 17 (2018). https://doi.org/10.1007/s10404-018-2039-3
66. Otomo, T., Noh, H., Matsubara, T., Kim, D.-H., Ikeuchi, M., Yoshida, K., Kim, J.-W.: Fabrication of biomimetic cell culture membranes using robust and reusable nickel micropillar molds. Biochip J. (2024). https://doi.org/10.1007/s13206-024-00179-7
67. Salvo, P., Verplancke, R., Bossuyt, F., Latta, D., Vandecasteele, B., Liu, C., Vanfleteren, J.: Adhesive bonding by SU-8 transfer for assembling microfluidic devices. Microfluid. Nanofluid. **13**, 987–991 (2012). https://doi.org/10.1007/s10404-012-1011-x
68. https://www.norlandprod.com/adhesives/noa86h.html. Accessed 28 June 2024.
69. Mokkapati, V.R.S.S., Bethge, O., Hainberger, R. Brueckl, H.: In 2012 IEEE 62nd Electronic Components and Technology Conference pp. 1965–1969 (2012)
70. Yin, J., Kuhn, S.: Numerical simulation of droplet formation in a microfluidic T-junction using a dynamic contact angle model. Chem. Eng. Sci. **261**, 117874 (2022). https://doi.org/10.1016/j.ces.2022.117874
71. Li, J., Liang, C., Zhang, H., Liu, C.: Reliable and high quality adhesive bonding for microfluidic devices. Micro Nano Lett. **12**, 90–94 (2017). https://doi.org/10.1049/mnl.2016.0478
72. Huang, Z., Sanders, J.C., Dunsmor, C., Ahmadzadeh, H., Landers, J.P.: A method for UV-bonding in the fabrication of glass electrophoretic microchips. Electrophoresis **22**, 3924–3929 (2001). https://doi.org/10.1002/1522-2683(200110)22:18%3c3924::AID-ELPS3924%3e3.0.CO;2-4
73. Lai, S., Cao, X., Lee, L.J.: A packaging technique for polymer microfluidic platforms. Anal. Chem. **76**, 1175–1183 (2004). https://doi.org/10.1021/ac034990t
74. Gong, H., Beauchamp, M., Perry, S., Woolley, A.T., Nordin, G.P.: Optical approach to resin formulation for 3D printed microfluidics. RSC Adv. **5**, 106621–106632 (2015). https://doi.org/10.1039/C5RA23855B
75. Cai, R., Luo, X., Xie, G., Wang, K., Peng, Y., Rao, Y.: Effects of the printing parameters on geometric accuracy and mechanical properties of digital light processing printed polymer. J. Mater. Sci. **59**, 14807–14819 (2024). https://doi.org/10.1007/s10853-024-10018-7
76. Sanchez Noriega, J.L., Chartrand, N.A., Valdoz, J.C., Cribbs, C.G., Jacobs, D.A., Poulson, D., Viglione, M.S., Woolley, A.T., Van Ry, P.M., Christensen, K.A., Nordin, G.P.: Spatially and optically tailored 3D printing for highly miniaturized and integrated microfluidics. Nat. Commun. **12**, 5509 (2021). https://doi.org/10.1038/s41467-021-25788-w
77. Gong, H., Bickham, B.P., Woolley, A.T., Nordin, G.P.: Custom 3D printer and resin for 18 μm × 20 μm microfluidic flow channels. Lab Chip **17**, 2899–2909 (2017). https://doi.org/10.1039/C7LC00644F
78. Vedhanayagam, A., Golfetto, M., Ram, J.L., Basu, A.S.: Rapid micromolding of sub-100 μm microfluidic channels using an 8K stereolithographic resin 3D printer. Micromachines **14**, 1519 (2023). https://doi.org/10.3390/mi14081519
79. Böcherer, D., Li, Y., Rein, C., Franco Corredor, S., Hou, P., Helmer, D.: High-resolution 3D printing of dual-curing thiolene/epoxy system for fabrication of microfluidic devices for bioassays. Adv. Funct. Mater. **34**, 2401516 (2024). https://doi.org/10.1002/adfm.202401516
80. Serra, M., Pereiro, I., Yamada, A., Viovy, J.L., Descroix, S., Ferraro, D.: A simple and low-cost chip bonding solution for high pressure, high temperature and biological applications. Lab Chip **17**, 629–634 (2017). https://doi.org/10.1039/C6LC01319H
81. Chung, A.J.: A minireview on inertial microfluidics fundamentals: inertial particle focusing and secondary flow. Biochip J. **13**, 53–63 (2019). https://doi.org/10.1007/s13206-019-3110-1
82. Wang, L., Dandy, D.S.: High-throughput inertial focusing of micrometer- and sub-micrometer-sized particles separation. Adv. Sci. **4**, 1700153 (2017). https://doi.org/10.1002/advs.201700153
83. Martel, J.M., Toner, M.: Inertial focusing in microfluidics. Annu. Rev. Biomed. Eng. **16**, 371–396 (2014). https://doi.org/10.1146/annurev-bioeng-121813-120704
84. Mutlu, B.R., Edd, J.F., Toner, M.: Oscillatory inertial focusing in infinite microchannels. Proc. Natl. Acad. Sci. U.S.A. **115**, 7682–7687 (2018). https://doi.org/10.1073/pnas.1721420115
85. Choi, S., Kang, B., Shimanouchi, T., Kim, K., Jung, H.: Continuous preparation of bicelles using hydrodynamic focusing method for bicelle to vesicle transition. Micro Nano Syst. Lett. **9**, 7 (2021). https://doi.org/10.1186/s40486-021-00133-4
86. Di Carlo, D., Irimia, D., Tompkins, R.G., Toner, M.: Continuous inertial focusing, ordering, and separation of particles in microchannels. Proc. Natl. Acad. Sci. U.S.A. **104**, 18892–18897 (2007). https://doi.org/10.1073/pnas.0704958104
87. Zhang, J., Li, W., Alici, G.: Inertial microfluidics: mechanisms and applications. In: Zhang, D., Wei, B. (eds.) Advanced Mechatronics and MEMS Devices II, pp. 563–593. Springer International Publishing, Cham (2017)
88. Lee, C., Chen, Y., Wang, P., Wallace, D.C., Burke, P.J.: A three-dimensional printed inertial microfluidic platform for isolation of minute quantities of vital mitochondria. Anal. Chem. **94**, 6930–6938 (2022). https://doi.org/10.1021/acs.analchem.1c03244
89. Di Carlo, D.: Inertial microfluidics. Lab Chip **9**, 3038–3046 (2009). https://doi.org/10.1039/B912547G

90. Baroud, C.N., Gallaire, F., Dangla, R.: Dynamics of microfluidic droplets. Lab Chip **10**, 2032–2045 (2010). https://doi.org/10.1039/C001191F
91. Amirifar, L., Besanjideh, M., Nasiri, R., Shamloo, A., Nasrollahi, F., de Barros, N.R., Davoodi, E., Erdem, A., Mahmoodi, M., Hosseini, V., Montazerian, H., Jahangiry, J., Darabi, M.A., Haghniaz, R., Dokmeci, M.R., Annabi, N., Ahadian, S., Khademhosseini, A.: Droplet-based microfluidics in biomedical applications. Biofabrication **14**, 022001 (2022). https://doi.org/10.1088/1758-5090/ac39a9
92. Zhu, P., Wang, L.: Passive and active droplet generation with microfluidics: a review. Lab Chip **17**, 34–75 (2017). https://doi.org/10.1039/C6LC01018K
93. Rosenfeld, L., Lin, T., Derda, R., Tang, S.K.Y.: Review and analysis of performance metrics of droplet microfluidics systems. Microfluid. Nanofluid. **16**, 921–939 (2014). https://doi.org/10.1007/s10404-013-1310-x
94. Lashkaripour, A., Rodriguez, C., Ortiz, L., Densmore, D.: Performance tuning of microfluidic flow-focusing droplet generators. Lab Chip **19**, 1041–1053 (2019). https://doi.org/10.1039/C8LC01253A
95. Lee, W., Kwon, D., Choi, W., Jung, G.Y., Au, A.K., Folch, A., Jeon, S.: 3D-printed microfluidic device for the detection of pathogenic bacteria using size-based separation in helical channel with trapezoid cross-section. Sci. Rep. **5**, 7717 (2015). https://doi.org/10.1038/srep07717
96. Sochol, R.D., Sweet, E., Glick, C.C., Venkatesh, S., Avetisyan, A., Ekman, K.F., Raulinaitis, A., Tsai, A., Wienkers, A., Korner, K., Hanson, K., Long, A., Hightower, B.J., Slatton, G., Burnett, D.C., Massey, T.L., Iwai, K., Lee, L.P., Pister, K.S.J., Lin, L.: 3D printed microfluidic circuitry via multijet-based additive manufacturing. Lab Chip **16**, 668–678 (2016). https://doi.org/10.1039/C5LC01389E
97. Huang, K., Matsumura, H., Zhao, Y., Herbig, M., Yuan, D., Mineharu, Y., Harmon, J., Findinier, J., Yamagishi, M., Ohnuki, S., Nitta, N., Grossman, A.R., Ohya, Y., Mikami, H., Isozaki, A., Goda, K.: Deep imaging flow cytometry. Lab Chip **22**, 876–889 (2022). https://doi.org/10.1039/D1LC01043C